

www.acsnano.org

# Giant Superelastic Piezoelectricity in Flexible Ferroelectric BaTiO<sub>3</sub> Membranes

Hemaprabha Elangovan, <sup>⊥</sup> Maya Barzilay, <sup>⊥</sup> Sahar Seremi, <sup>⊥</sup> Noy Cohen, Yizhe Jiang, Lane W. Martin, and Yachin Ivry\*



Cite This: ACS Nano 2020, 14, 5053-5060



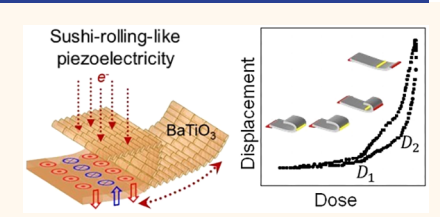
**ACCESS** 

III Metrics & More



Supporting Information

ABSTRACT: Mechanical displacement in commonly used piezoelectric materials is typically restricted to linear or biaxial in nature and to a few percent of the material dimensions. Here, we show that free-standing BaTiO<sub>3</sub> membranes exhibit nonconventional electromechanical coupling. Under an external electric field, these superelastic membranes undergo controllable and reversible "sushi-rolling-like" 180° folding—unfolding cycles. This crease-free folding is mediated by charged ferroelectric domains, leading to giant >3.8 and 4.6  $\mu$ m displacements for a 30 nm thick membrane at room temperature and 60 °C, respectively. Further increasing the electric field



above the coercive value changes the fold curvature, hence augmenting the effective piezoresponse. Finally, it is found that the membranes fold with increasing temperature followed by complete immobility of the membrane above the Curie temperature, allowing us to model the ferroelectric domain origin of the effect.

**KEYWORDS:** flexible piezoelectrics, flexible ferroelectrics, piezoelectric membrane, ferroelectric membrane, crease-free folding, in situ microscopy

he electromechanical power conversion of piezoelectrics is the basis for a broad range of sensing, actuating, and communication technologies, including ultrasound imaging and cellular phones. 1-3 Recent interest in electromechanical energy harvesting<sup>4,5</sup> as well as in flexible electronics for wearable devices, 6,7 nanomotors, 8 and medical applications 9-11 raises a need for flexible piezoelectric materials and devices. Modern applications of piezoelectrics hinge on thin films; 12-14 however, the substrate in such geometries is typically rigid, preventing the development of flexible devices. Flexible piezoelectric devices are therefore based on either nanowires<sup>4</sup> or thin-film systems but with substrates that have been designed especially for such applications. 15,16 Most piezoelectric applications rely on leadbased materials, which exhibit strong piezoelectric coefficients. Nevertheless, the toxicity of these materials is undesirable for environmental considerations, whereas it also disqualifies them for medical or wearable applications. Likewise, traditional thinfilm geometries limit the electromechanical excitation modes. That is, usually, a uniaxial electric field results in either parallel or perpendicular uniaxial or biaxial mechanical deformation (or vice versa). Nevertheless, the interest in flexible electronic technologies raises a need for advanced electromechanical excitation modes, such as for motorized devices, including microscale aerial vehicles.11

Substrate removal for piezoelectric films or membranes augments their functional properties, <sup>18–21</sup> mainly due to mechanically induced ferroic domain reorganization. <sup>22</sup> How-

ever, the preparation of completely stand-alone substrate-free films has remained a challenge. Lu et al.<sup>23</sup> demonstrated recently a general method to prepare oxide materials in the form of membranes, that is, continuous free-standing thin films with no substrate. More recently, Dong et al. 24 used this method to process BaTiO<sub>3</sub> membranes, which is a well-known lead-free piezoelectric and ferroelectric material. This work showed exceptional elastic and flexible properties that arise from the irregular ferroelectric domain dynamics in these membranes. Nevertheless, the piezoelectric properties of freestanding membranes have remained elusive. Here, we fabricated a flexible free-standing piezoelectric BaTiO<sub>3</sub> film. We show that, under external electric fields, the membrane folds gradually and continuously by 180°, similar to the rolling of a sushi roll with a bamboo makisu mat. The fold-unfold cycles are reversible and reproducible. We used this makisulike piezoelectric effect to fold a 30 nm thick membrane for a length that is greater than 4.6  $\mu$ m. We demonstrate the temperature dependence of this unexpected electromechanical coupling mode, indicating that the effect is dominated by the

Received: February 24, 2020 Accepted: April 9, 2020 Published: April 9, 2020





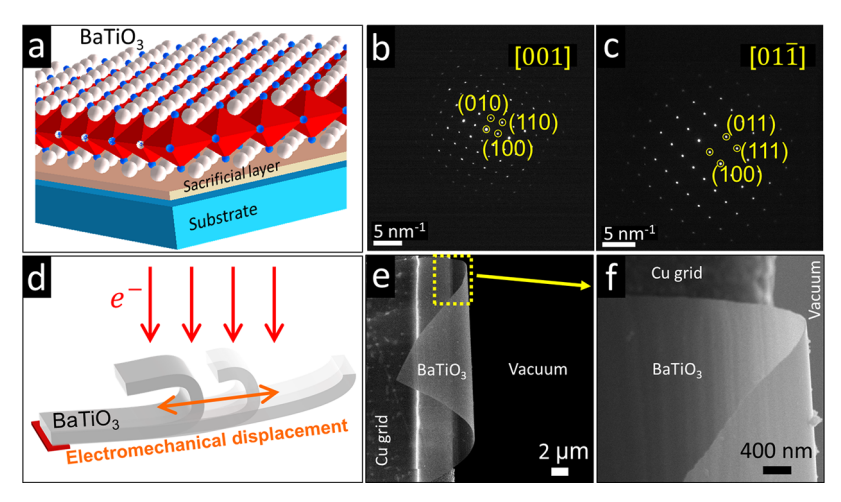


Figure 1. Foldable single-crystal BaTiO<sub>3</sub> membrane. (a) Schematic of the single-crystal (001)-oriented BaTiO<sub>3</sub> membrane on the water-soluble sacrificial layer above the SrTiO<sub>3</sub> substrate, from which the membrane was extracted. Diffraction patterns of a 30 nm thick BaTiO<sub>3</sub> membrane from (b)  $\begin{bmatrix} 001 \end{bmatrix}$  and (c)  $\begin{bmatrix} 011 \end{bmatrix}$  zone axes, showing the single-crystal tetragonal structure (a = b = 3.95 Å are the pseudocubic lattice constants). (d) Schematics of the folded membrane at the native state as well as its electromechanical rolling and unfolding response under an electron-beam-induced field. (e) Scanning electron microscope (SEM) micrographs of the natively folded BaTiO<sub>3</sub> membrane and (f) a closer look micrograph from the fold region.

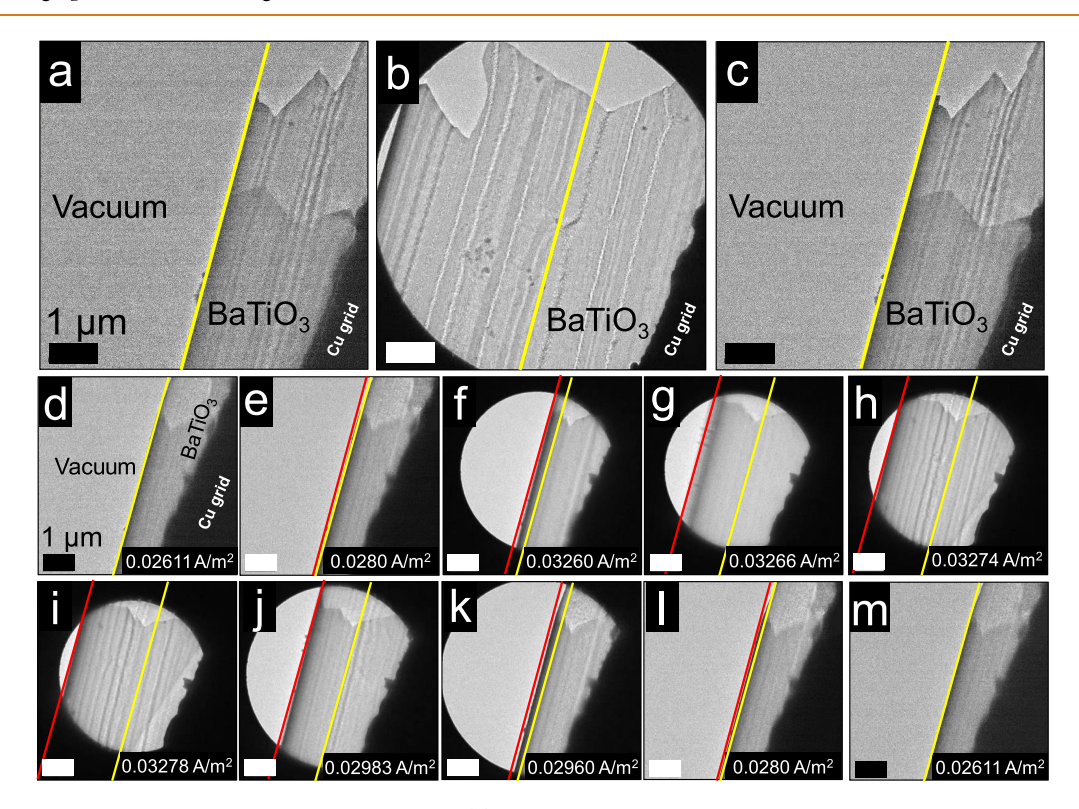


Figure 2. Makisu-like folding cycle in BaTiO<sub>3</sub> membranes. (a) TEM image of 30 nm thick BaTiO<sub>3</sub> membrane in its native state. The membrane is folded over itself at one edge and is tethered to the copper grid at its other edge (sample #1). (b) At high dose values ( $D = 0.0337 \text{ A/m}^2$ ), the membrane unfolds so that the structure extends to 3.75  $\mu$ m. (c) When the electric field is reduced again, the membrane folds back to its initial state. (d-h) Representative TEM micrographs of an unfold process as a result of increasing dose. For low-dose values, there is nearly no change in the fold (d,e). At an intermediate dosage (f), above the threshold value  $D_1$ , the membrane unfolds while maintaining a constant radius of curvature at the fold, as in the case of sushi rolling. Finally, at high doses (above  $D_2$ ), the sample unfolds abruptly with increasing electric field due to variation in the curvature at the fold (g,h), completing a three-step electromechanical response. (i-m) Electromechanical folding response as a function of decreasing dose showing the reversibility of the effect in the complete unfolding—folding cycle.

polarization domains. Based on the thorough quantification of the electromechanical folding dynamics, we present a model that explains the domain origin of this unconventional piezoelectric effect.

## **RESULTS AND DISCUSSION**

Free-standing single-crystal  $BaTiO_3$  30 nm thick membranes were prepared by pulsed-laser deposition when using a sacrificial layer that was dissolved in water (Figure 1a; see

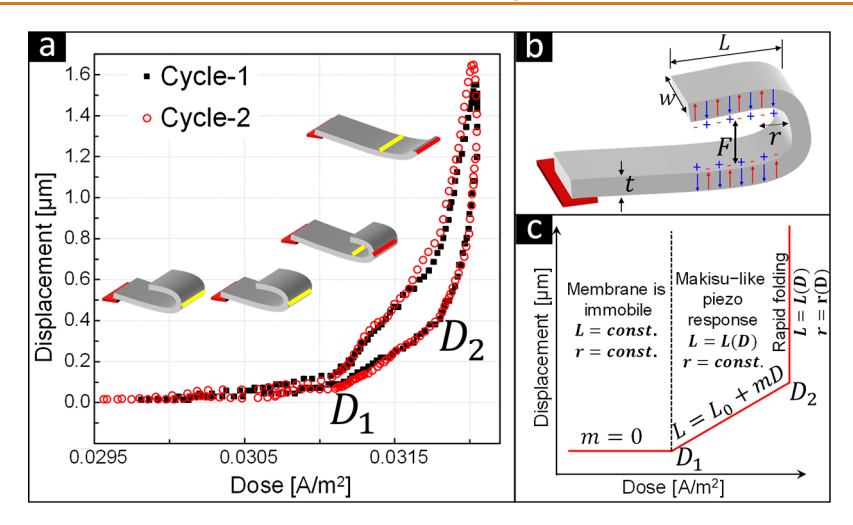


Figure 3. Electromechanical cycles in BaTiO<sub>3</sub>. (a) Displacement of the membrane fold front *versus* dose (equivalent to electric field) for two cycles shows reversible and reproducible electromechanical response (data extracted from sample #2). With increasing dosage, the fold remains unchanged in its native state until the value exceeds  $D_1$ . At intermediate dosage  $(D_2 > D > D_1)$ , the membrane unfolds with linear dependence of the displacement on the dose similarly to the makisu mat motion during sushi rolling. When the dose reaches a threshold value  $(D_2)$ , the membrane unfolds abruptly. Decreasing the dosage results is reversible piezoresponse, whereas repeating the electromechanical cycle demonstrates no apparent change in the reproducible piezoresponse. Additional data from three more samples are given in Video S4 to show the reproducibility of the effect. Schematic illustration of the membrane's electromechanical structure is given in (b), and illustration of the membrane fold for representative dose values that correspond to the micrographs in the figure are overlaid in (a). (c) Simplified description of the piezoresponse cycle.

Methods for details as well as in Figure S1). The pseudocubic perovskite structure of the single crystal was confirmed by electron diffraction (Figure 1b,c). Membranes were folded in their native state, as illustrated both schematically (Figure 1d) and by scanning electron micrographs (Figure 1e,f). The samples were put on transmission electron microscope (TEM) carbon-free (100  $\mu$ m) copper mesh and were plasma cleaned. We used the TEM to exert an electric field on the membrane *in situ* and image the resultant inverse piezoresponse. Here, the electric field was adjusted by changing the electron-beam flux or dose (D) controllably, allowing quantitative measurements of the mechanical deformation. Details regarding the dose calibration and data acquisition are given in the Methods section.

Figure 2 shows the membrane dynamics under several representative dose values (the complete dynamics are given in Videos S1 and S2). Figure 2a shows that, initially, at the native state, the membranes are folded. The bottom part of the membrane is tethered by the copper grid. At the other side, the edge of the membranes is folded over itself (*i.e.*, 180°), forming a top layer with an overlap of a length  $L_0$ . Upon increasing the electric field ( $D = 0.0337 \text{ A/m}^2$ ), the membrane unfolds and opens by >3.8  $\mu$ m, as seen in Figure 2b (4.2  $\mu$ m unfold was estimated from Video S1). This length is more than 2 orders of magnitude larger than the 30 nm thickness of the membrane. When the field is decreased, the membrane folds back to its initial native state (Figure 2c).

To characterize the electromechanical response over a complete unfold—fold period, we imaged and measured the mechanical displacement of the membrane under continuous variable electric-field conditions. The native membrane here is given in Figure 2d, where the top part is folded above the edge of the bottom part of the membrane. This fold remains constant even upon increasing the dose value, as long as the dose does not exceed a certain threshold value,  $D_1$  (Figure 2e). When the dose is increased above  $D_1$ , the membrane unfolds continuously (Figure 2g,h). The unfolding is reminiscent of

sushi rolling on a bamboo makisu mat, as seen in Figure 2. The electromechanical response of the makisu-like effect is reversible, with a small hysteresis between the unfolding and folding paths, whereas no crease is observed during or after the fold. The folding as a result of dose decrease is given in Figure 2i—m, completing the reversible unfolding—folding electromechanical response cycle.

To quantify the electromechanical response, we recorded the position of the fold and plotted this value as a function of dose (Figure 3a). The complete piezoresponse of this cycle is given in Video S3. Figure 3a shows a clear distinction between the fold behavior at different dosage values. Below  $D_1$ , the membrane remains at its native state and there is no change in the folded length  $(L_0)$ . At the intermediate dosage, between  $D_1$ and  $D_2$  (during the makisu-like rolling), the displacement of the fold front, or the length of the unfolding segment (designated with L in Figure 3b), varies linearly with increasing dosage. The fold is thus described by  $L = L_0 + mD$ , where m is a constant and  $L_0$  and m are measurable. Here, the radius of curvature remains constant, so that the membrane rolls and the top and bottom parts of the membrane that are far from the fold look like sliding to opposite directions. At the second threshold dosage value,  $D_2$ , the membrane unfolds abruptly, nonlinearly with increasing dosage. Here, the rapid unfold occurs due to a significant sudden change in the curvature. Figure 3a shows also the reversible three-step effect, in which the membrane folds back toward its native state, when the dosage is decreased. Schematic illustration of the membrane state is overlaid on Figure 3a for several dose values. The threestep electromechanical response is depicted schematically in Figure 3c (see also Video S3 for the experimental data that correspond to the three-step process).

We then confirmed the reproducibility of this piezoresponse by performing a sequential unfold—fold cycle, as presented in Figure 3a (the complete cycles are given visually in Video S3). The observed reproducibility of the electromechanical cycles suggest that the fold does not involve creases. The universality

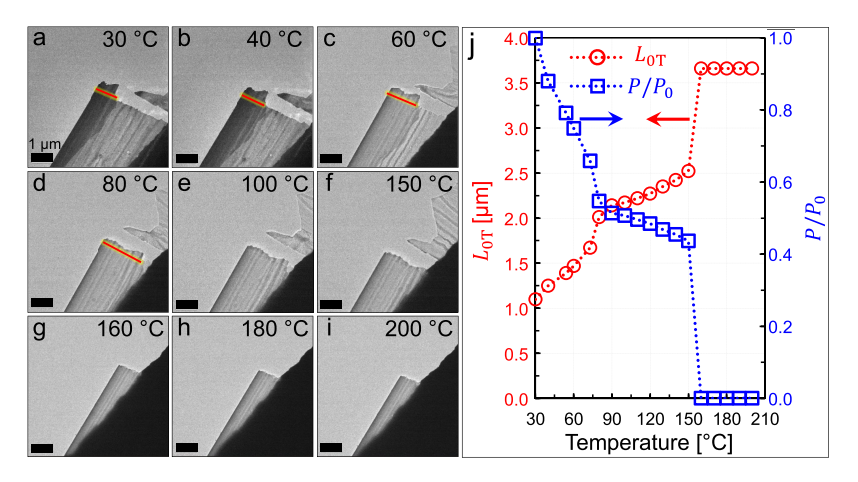


Figure 4. Temperature dependence of the native fold in a BaTiO<sub>3</sub> membrane. (a–f) TEM micrographs of the native membrane ( $D \ll D_1$ ) with in situ temperature variation shows an increase of the folded segment ( $L_0$ ) with increasing temperature, for temperatures up to 150 °C (i.e., the Curie temperature). (g–i) Above 150 °C, the native fold did not change with temperature. Dose variation for the different temperatures (Video S5) show that the membrane undergoes electromechanical cycles up to 150 °C, and above this temperature, the membrane remains immobile. (k) Temperature dependence of the native fold length ( $L_{0T}$ ) as well as of the corresponding calculated polarization (see eq 2).

of this effect was also confirmed by observing it in more than five different samples (Video S4 demonstrates such a typical measurement).

We then wanted to expose the origin of the giant electromechanical response. The change in dose may result in mechanical response due to irradiation effects, such as heating or damage. Such effects are examinable because they are accompanied by a strong influence of the exposure time on the mechanical motion. 27 That is, the accumulated charge or power, not the flux or dose, are the driving excitations. Alternatively, if the effect is electromechanical, that is, due to piezoelectricity, there should be a dependence only on the electric field or dose value<sup>28,29</sup> and not on the exposure time. We thus examined the dependence of the mechanical response on exposure time. We increased significantly the wait time whenever the dose was changed. Figure S2 shows that, upon changing the dose, the sample unfolded only for a short time (2-3 s), whereas increasing the exposure time beyond this time constant, for a given dose, resulted in no mechanical change in the fold. To further verify that the electromechanical effect is truly piezoelectric in nature, one should demonstrate dependence of the effect on the piezoelectric and perhaps also on the ferroelectric properties of the material. Piezoelectricity stems from the lack of inversion symmetry in the crystal structure. Although BaTiO3 is polar and piezoelectric at room temperature, it undergoes a structural phase transformation at a Curie temperature (200 °C >  $T_{\rm C}$  > 100 °C). Thus, above this Curie temperature  $(T_C)$ , the crystal becomes centrosymmetric, eliminating piezoelectricity and ferroelectricity. To illustrate that the observed electromechanical response is piezoelectricity, one has therefore to confirm that the effect is absent above  $T_{\rm C}$ .

Figure 4 shows the fold evolution of the membrane as a function of *in situ* temperature variation (double-tilt heating holder, Gatan Inc. model 652), whereas complete unfold—fold cycles for various temperatures are given in Video S5. In Figure 3, the dose was held constant, so that the effect of temperature was isolated. The data clearly show that, below 160 °C (Figure 4a–f), the length of the native membrane fold ( $L_0$ ) increased with increasing temperature. Above  $T=150\,$  °C, no electromechanical folding occurred (Figure 4g–i). Figure 4j

shows quantification of the microscopy observations, where the temperature-dependent native fold  $(L_{0T})$  is plotted as a function of temperature. Below  $T_{C_i}$  the piezoresponse cycles are similar to the room temperature behavior of Figures 2 and 3. Because the initial fold  $(L_{0T})$  increased with increasing temperature, complete opening of the membrane gave rise to displacements larger than those recorded at room temperature, with a maximal displacement length of 4.6 µm. However, above  $T_C$ , the membrane became immobile and neither unfolded nor folded with dose variation. Therefore, not only do these results demonstrate that the electromechanical coupling is not heat driven, but they also confirm that the effect is based on the membrane's piezoelectric and ferroelectric properties. Note that the linear response at  $D_2 > D$  $D_1$  also indicates that the electromechanical response is piezoelectricity.

A "sushi-rolling-like" motion does not usually occur in continuous structures in nature, and it requires the motion of discrete jointed elements, similar to the motion of the discrete bamboo sticks in a makisu mat or to the motion of inch-worm motors. Moreover, the temperature dependence of the fold (Figure 4j) is reminiscence of the dependence of polarization on temperature in ferroelectrics. Hence, one can assume that the folding—unfolding piezoresponse emerges from the discrete polarization distribution, which follows the domain structure along the membrane. This assumption receives strong support from the recent work of Dong *et al.*, <sup>24</sup> in which the effect of polarized ferroelectric domains on the elastic properties of such membranes was found to be crucial.

Here, we propose that the top and bottom parts of the fold are being held by attractive electric forces that compensate for the stress, which is developed by the curved fold. The electromechanical motion is possible due to the existence of ferroelectric domains with a finite width. Following Roytburd's model,  $^{32}$  a 30 nm thick membrane has 28 nm domain periodicity. That is, domains from the top and bottom parts of the membrane form surface charge with opposite polarity, forming an effective plate capacitor (see Supporting Information for details of the model derivation). The two charged surfaces attract each other, due to a force between opposite domains with width w, length l, and surface charge  $\sigma$ ,

which is given by  $F_{p^{\pm}}=\frac{wl}{\epsilon_0\varepsilon}\sigma^2$ . Here,  $\epsilon_0$  is the vacuum permittivity, and  $\epsilon$  is the dielectric constant of the medium between the two parts of the membrane.

The total force between all domains should sum up to the mechanical force that is required to bend a membrane with Young's modulus<sup>33</sup> Y and a thickness t in a radius of curvature r. Thus, we obtain a direct relationship between the surface charge and the length of the fold:

$$\sigma = \frac{1}{L} \sqrt{\frac{\epsilon \epsilon_0 Y t^3}{6r}} \tag{1}$$

That is, increasing the dose, which gives rise to a decrease in L (see Figure 3c), stems from an increase in the surface charge. Presumably, the electromechanical effect was related to direct electron charging; however, the absence of a dependence of the electromechanical effect on time exposure suggests that the effect is not due to direct charge injection. We may therefore attribute the surface charge,  $\sigma$ , broadly to the out-of-plane domain polarization, P.

At the native state  $(D < D_1)$ , the surface charge corresponds to P.<sup>34</sup> Applying a dose is equivalent to exerting an external electric field on the membrane due to the high dielectric constant of ferroelectrics. <sup>28,29,35</sup> High electric field and hence high doses are expected to allow polarization switching, whereas electric-field gradients may also induce similar effects due to flexoelectricity. Typically, for dc fields, there is no time dependence (beyond a certain Debye time constant) of the domain distribution for a given electric field.<sup>38</sup> When the dose increases, the polarization changes to reduce the global electromechanical free energy of the system. This change occurs gradually at first  $(D_2 > D > D_1)$ . At a certain threshold value  $(D = D_2)$ , the polarization changes abruptly, suggesting that  $D_2$  is equivalent to the global coercive electric field (expected to be around 2 V for our membrane).<sup>24</sup> This analysis complies with existing models that show that domains in freestanding BaTiO<sub>3</sub> membranes are rather easily switchable.<sup>24</sup> Hence, we can deduce the dependence of polarization on the observable fold length for doses smaller than  $D_2$  as

$$\frac{P}{P_0} = \frac{L_0}{L} \tag{2}$$

Note that for doses  $D_2 > D > D_1$ , L changes linearly with the dose (Figure 3a,c), so that the dependence of P on D can be expressed directly. Moreover, eq 1 is valid for the polarization dependence on L also at higher-dose values, above  $D_2$ . However, in this regime, the radius of curvature changes, adding an unknown free parameter to the system, and the exact fitting of the experimental results becomes more challenging. Likewise, we should note that, for such high doses, the effect of direct charging by the beam—not necessarily of the membrane but also of surface adsorbents  $^{39}$ —may become meaningful, also effectively affecting  $\epsilon$ .

Equation 2 allows us to analyze the temperature dependence experiment (Figure 4). Here, the initial fold at the native state  $(L_{0\mathrm{T}})$  increases with increasing temperature. Substituting L with  $L_{0\mathrm{T}}$  in eq 2 allows us to plot the temperature dependence of the polarization in the membrane (Figure 4k). That is, the decrease in polarization with temperature reduces the surface charge and hence increases  $L_{0\mathrm{T}}$ , whereas above  $T_{\mathrm{C}}$ , there is no polarization and  $L_{0\mathrm{T}}$  remains constant. Of course, for temperatures higher than  $T_{\mathrm{C}}$ , eq 2 is not valid. Yet, surface

charge and charged adsorbents may still give rise to a fold, following eq 1. Here, there are no domains that change with dose, and hence there should not be any folding effect. These conclusions are in agreement with the experimental observations in Video S5. Similarly, Video S6 shows temperature reversibility of the electromechanical folding.

#### **CONCLUSIONS**

As a final remark, we would like to summarize our observations in the light of possible future applications and research directions. The electromechanical response as well as the unexpected functionality of the piezoelectric-ferroelectric freestanding membranes presented here is applicable for a broad range of devices and technologies, including at the micrometer and nanometer scale. These devices are completely different from piezoelectric systems that are based on bulk materials or on thin films. The reversible crease-free and a "sushi-rollinglike" folding are exceptional mechanical motions that do not usually exist in continuous materials in nature and invite further investigation. The demonstrated reversible and reproducible behavior is promising for robust motors and actuators with high-precision controllability. Likewise, the temperature dependence of the makisu-like piezoresponse can be utilized for temperature-driven actuators, sensors, and motors. In addition, the present demonstration of contact-less electromechanical actuation enables contact-less piezoelectric devices that do not require constant voltage contacts and can be operated remotely, which is important in environments that do not allow electric wiring. Likewise, the domain-driven giant electromechanical response presented here experimentally and theoretically deserves further insight into the fundamental mechanism, whereas seeking additional systems that utilize this effect may result in technologically and scientifically advantageous materials.

# **EXPERIMENTAL METHODS**

Thin-Film Deposition. To produce the free-standing films, we first optimized the growth of BaTiO<sub>3</sub>/SrTiO<sub>3</sub>(001) heterostructures using pulsed-laser deposition with a KrF excimer laser (248 nm, Compex, Coherent), in an on-axis geometry. X-ray diffraction studies (Figure S1a) reveal the ability to produce high-quality, fully epitaxial films of BaTiO<sub>3</sub>. In turn, to produce the free-standing films, 30 nm BaTiO<sub>3</sub>/20 nm La<sub>0.7</sub>Sr<sub>0.3</sub>MnO<sub>3</sub>/SrTiO<sub>3</sub>(001) heterostructures were grown via pulsed-laser deposition. The La<sub>0.7</sub>Sr<sub>0.3</sub>MnO<sub>3</sub> films that served as a sacrificial etching layer for the subsequent release of the film from the substrate were grown directly on the SrTiO<sub>3</sub>(001) single-crystal substrates (Crystec, GmbH) from a ceramic La<sub>0.7</sub>Sr<sub>0.3</sub>MnO<sub>3</sub> target, at a heater temperature of 650 °C in a dynamic oxygen pressure of 200 mTorr at a laser repetition rate of 3 Hz and a laser fluence of 1.03 J cm<sup>-2</sup>. The BaTiO<sub>3</sub> films were grown from a BaTiO<sub>3</sub> ceramic target at a heater temperature of 600 °C in a dynamic oxygen pressure of 40 mTorr at a 2 Hz laser repetition rate and a laser fluence of 1.14 J cm<sup>-2</sup>. The substrates were adhered to the heater with silver paint (Ted Pella, Inc.). Following growth, the heterostructures were cooled to room temperature at a rate of 10 °C  $min^{-1}$  in a static oxygen pressure of ~700 Torr. Details regarding the BaTiO<sub>3</sub> film deposition and the membrane processing are in Figure

Film Release and Transfer to a TEM Grid. After growth, the  $BaTiO_3$  films were released from the substrate by selective etching of the sacrificial  $La_{0.7}Sr_{0.3}MnO_3$  layer. The etching process requires that the heterostructures will be placed in an aqueous solution of 8 mg of KI + 10 mL of HCl + 100 mL of H<sub>2</sub>O; this solution results in a high etch rate for  $La_{0.7}Sr_{0.3}MnO_3$ , while having negligible impact on the  $BaTiO_3$  films (i.e., etch rate of  $La_{0.7}Sr_{0.3}MnO_3$  is much greater than the

etch rate of BaTiO<sub>3</sub>). After the La<sub>0.7</sub>Sr<sub>0.3</sub>MnO<sub>3</sub> was selectively etched, the released BaTiO<sub>3</sub> thin films were observed to sit on the substrate. The unclamped thin films were then removed from the substrate by slowly dipping the substrate in deionized water. When done correctly, the released films float on the water surface (Figure S1b). A nichrome wire loop (Ted Pella, Inc.) was then used to "catch" the free-standing BaTiO<sub>3</sub> films from the water surface (Figure S1c). The films were held in place by a thin layer of water which was formed inside the metal loop. The released films were then moved to a secondary substrate (i.e., a 100 mesh carbon-free copper TEM grid, Ted Pella, Inc.). A piece of filter paper was placed underneath the TEM grid, so that when the loop came close to the grid the water inside the loop was absorbed by the paper, thus leaving the film on the TEM grid (Figure S1d). Tapping mode (AC Air) atomic force microscopy studies of the BaTiO<sub>3</sub> surfaces before and after release show no changes in topography and root mean square roughness, which remained around 400 pm.

Dose Calibration and Data Acquisition. The condenser-2 (C2) lens strength of the TEM determines the electron dose (following ref 27). Therefore, by changing the strength of the C2 lens (using intensity knob), the electron dose has been increased or decreased.

The TEM software presents the measured dose value, which is obtained by integrating the intensity of the beam falling on the fluorescent screen. During imaging and video recording, the electron beam that goes through the sample falls on the camera and not on the fluorescent screen. Therefore, only the C2 lens strength will be indicated in the software during imaging. Hence, dose value correspondence to the C2 lens strength is captured by allowing the beam to fall on the fluorescent screen. Later, the mechanical motion has been recorded along with the C2 lens strength when allowing the beam to fall on the camera. The C2 lens strength and the dose value have been interpolated from these two experiments.

**Structural Characterization.** Structural studies were performed using high-resolution X-ray diffraction (Panalytical, X'pert3MRD) 9 kW diffractometer. A Cu K $\alpha$  rotating-anode source at 45 kV was used, with a 200 mA tube current. TEM studies were performed using a Technai T20 microscope equipped with LaB<sub>6</sub> thermionic emission gun operated at 200 keV. The TEM samples were plasma cleaned under an Ar + O<sub>2</sub> atmosphere for 10 s prior to being inserted into the TEM. The SEM micrographs were acquired using Zeiss Ultra-Plus FEG-SEM operated at a 4 keV (Figure 1e) and a 20 keV (Figure 1f) acceleration voltage.

# **ASSOCIATED CONTENT**

## Supporting Information

The Supporting Information is available free of charge at https://pubs.acs.org/doi/10.1021/acsnano.0c01615.

X-ray diffraction profile of  $BaTiO_3$  film; film release process; time dependence study of the electromechanical folding—unfolding experiment under nearly constant electron dosage; derivation of the model for surface charge and the parameters employed in the related calculations (PDF)

Video S1: Folding—unfolding cycle under variable dosage captured for sample #1 (MP4)

Video S2: Electromechanical unfolding—folding cycle under variable dosage captured for sample #4 (MP4) Video S3: Two consecutive electromechanical unfolding—folding cycles and plotted displacement under variable dosage for sample #2 (MP4)

Video S4: Reproducible folding—unfolding electromechanical cycles for sample #3 and sample #5 (MP4) Video S5: Folding—unfolding cycles for sample #1 captured at different temperatures, below and above  $T_{\rm C}$  (MP4)

Video S6: Temperature reversibility of electromechanical folding—unfolding (MP4)

#### **AUTHOR INFORMATION**

## **Corresponding Author**

Yachin Ivry — Department of Materials Science and Engineering and Solid State Institute, Technion — Israel Institute of Technology, Haifa 3200003, Israel; ⊚ orcid.org/0000-0002-3045-923X; Email: ivry@technion.ac.il

#### **Authors**

Hemaprabha Elangovan – Department of Materials Science and Engineering and Solid State Institute, Technion – Israel Institute of Technology, Haifa 3200003, Israel

Maya Barzilay — Department of Materials Science and Engineering and Solid State Institute, Technion — Israel Institute of Technology, Haifa 3200003, Israel

Sahar Seremi — Department of Materials Science and Engineering, University of California, Berkeley, Berkeley, California 94720, United States; Materials Sciences Division, Lawrence Berkeley National Laboratory, Berkeley, California 94720, United States; orcid.org/0000-0002-1625-8036

Noy Cohen — Department of Materials Science and Engineering, Technion — Israel Institute of Technology, Haifa 3200003, Israel; ⊚ orcid.org/0000-0003-2224-640X

Yizhe Jiang — Department of Materials Science and Engineering, University of California, Berkeley, Berkeley, California 94720, United States; Materials Sciences Division, Lawrence Berkeley National Laboratory, Berkeley, California 94720, United States

Lane W. Martin — Department of Materials Science and Engineering, University of California, Berkeley, Berkeley, California 94720, United States; Materials Sciences Division, Lawrence Berkeley National Laboratory, Berkeley, California 94720, United States

Complete contact information is available at: https://pubs.acs.org/10.1021/acsnano.0c01615

# **Author Contributions**

<sup>⊥</sup>H.E., M.B., and S.S. contributed equally to this work.

#### Notes

The authors declare no competing financial interest.

# **ACKNOWLEDGMENTS**

The Technion team acknowledges support from the Zuckerman STEM Leadership Program and the Technion Russel Barry Nanoscience Institute, as well as from the Israel Science Foundation (ISF) Grant No. 1602/17. We would also like to thank Dr. Yaron Kauffman and Mr. Michael Kalina for technical support. S.S. acknowledges support from the National Science Foundation under Grant No. DMR-1708615. Y.J. acknowledges support from the U.S. Department of Energy, Office of Science, Office of Basic Energy Sciences, under Award No. DE-SC-0012375 for the development of free-standing ferroelectric materials. L.W.M. acknowledges support from the U.S. Department of Energy, Office of Science, Office of Basic Energy Sciences, Materials Sciences and Engineering Division under Contract No. DE-AC02-05-CH11231 (Materials Project Program KC23MP) for the development of functional ferroic materials.

## **REFERENCES**

- (1) Lang, C.; Fang, J.; Shao, H.; Ding, X.; Lin, T. High-Sensitivity Acoustic Sensors from Nanofibre Webs. *Nat. Commun.* **2016**, *7*, 11108
- (2) Yang, J.; Li, Z.; Xin, X.; Gao, X.; Yuan, X.; Wang, Z.; Yu, Z.; Wang, X.; Zhou, J.; Dong, S. Designing Electromechanical

- Metamaterial with Full Nonzero Piezoelectric Coefficients. Sci. Adv. 2019, 5, eaax1782.
- (3) Song, K.; Zhao, R.; Wang, Z. L.; Yang, Y. Conjuncted Pyro-Piezoelectric Effect for Self-Powered Simultaneous Temperature and Pressure Sensing. *Adv. Mater.* **2019**, *31*, 1902831.
- (4) Wang, Z. L.; Song, J. Piezoelectric Nanogenerators Based on Zinc Oxide Nanowire Arrays. *Science* **2006**, 312, 242–246.
- (5) Qi, Y.; Kim, J.; Nguyen, T. D.; Lisko, B.; Purohit, P. K.; McAlpine, M. C. Enhanced Piezoelectricity and Stretchability in Energy Harvesting Devices Fabricated from Buckled PZT Ribbons. *Nano Lett.* **2011**, *11*, 1331–1336.
- (6) Lee, J. H.; Lee, K. Y.; Gupta, M. K.; Kim, T. Y.; Lee, D. Y.; Oh, J.; Ryu, C.; Yoo, W. J.; Kang, C. Y.; Yoon, S. J.; Yoo, J. B.; Kim, S. W. Highly Stretchable Piezoelectric-Pyroelectric Hybrid Nanogenerator. *Adv. Mater.* **2014**, *26*, 765–769.
- (7) Lee, M.; Chen, C. Y.; Wang, S.; Cha, S. N.; Park, Y. J.; Kim, J. M.; Chou, L. J.; Wang, Z. L. A Hybrid Piezoelectric Structure for Wearable Nanogenerators. *Adv. Mater.* **2012**, *24*, 1759–1764.
- (8) Smith, G. L.; Pulskamp, J. S.; Sanchez, L. M.; Potrepka, D. M.; Proie, R. M.; Ivanov, T. G.; Rudy, R. Q.; Nothwang, W. D.; Bedair, S. S.; Meyer, C. D.; Polcawich, R. G. PZT-Based Piezoelectric MEMS Technology. J. Am. Ceram. Soc. 2012, 95, 1777–1792.
- (9) Wu, N.; Cheng, X.; Zhong, Q.; Zhong, J.; Li, W.; Wang, B.; Hu, B.; Zhou, J. Cellular Polypropylene Piezoelectret for Human Body Energy Harvesting and Health Monitoring. *Adv. Funct. Mater.* **2015**, 25, 4788–4794.
- (10) Chorsi, M. T.; Curry, E. J.; Chorsi, H. T.; Das, R.; Baroody, J.; Purohit, P. K.; Ilies, H.; Nguyen, T. D. Piezoelectric Biomaterials for Sensors and Actuators. *Adv. Mater.* **2019**, *31*, 1802084.
- (11) Dagdeviren, C.; Su, Y.; Joe, P.; Yona, R.; Liu, Y.; Kim, Y. S.; Huang, Y.; Damadoran, A. R.; Xia, J.; Martin, L. W.; Huang, Y.; Rogers, J. A. Conformable Amplified Lead Zirconate Titanate Sensors with Enhanced Piezoelectric Response for Cutaneous Pressure Monitoring. *Nat. Commun.* **2014**, *5*, 4496.
- (12) Wang, X.; He, X.; Zhu, H.; Sun, L.; Fu, W.; Wang, X.; Hoong, L. C.; Wang, H.; Zeng, Q.; Zhao, W.; Wei, J.; Jin, Z.; Shen, Z.; Liu, J.; Zhang, T.; Liu, Z. Subatomic Deformation Driven by Vertical Piezoelectricity from CdS Ultrathin Films. *Sci. Adv.* **2016**, 2, No. e1600209.
- (13) Saremi, S.; Xu, R.; Dedon, L. R.; Gao, R.; Ghosh, A.; Dasgupta, A.; Martin, L. W. Electronic Transport and Ferroelectric Switching in Ion-Bombarded, Defect-Engineered BiFeO<sub>3</sub> Thin Films. *Adv. Mater. Interfaces* **2018**, *5*, 1700991.
- (14) Dedon, L. R.; Saremi, S.; Chen, Z.; Damodaran, A. R.; Apgar, B. A.; Gao, R.; Martin, L. W. Nonstoichiometry, Structure, and Properties of BiFeO<sub>3</sub> Films. *Chem. Mater.* **2016**, *28*, 5952–5961.
- (15) Tsai, M. F.; Jiang, J.; Shao, P. W.; Lai, Y. H.; Chen, J. W.; Ho, S. Z.; Chen, Y. C.; Tsai, D. P.; Chu, Y. H. Oxide Heteroepitaxy-Based Flexible Ferroelectric Transistor. ACS Appl. Mater. Interfaces 2019, 11, 25882–25890.
- (16) Onn Winestook, R.; Saguy, C.; Ma, C. H.; Chu, Y. H.; Ivry, Y. Enhanced Ferroelectric Functionality in Flexible Lead Zirconate Titanate Films with *In Situ* Substrate-Clamping Compensation. *Adv. Electron. Mater.* **2019**, *5*, 1900428.
- (17) Jafferis, N. T.; Helbling, E. F.; Karpelson, M.; Wood, R. J. Untethered Flight of an Insect-Sized Flapping-Wing Microscale Aerial Vehicle. *Nature* **2019**, *570*, 491–495.
- (18) Choi, K. J.; Biegalski, M.; Li, Y. L.; Sharan, A.; Schubert, J.; Uecker, R.; Reiche, P.; Chen, Y. B.; Pan, X. Q.; Gopalan, V.; Che, L. Q.; Schlom, D. C.; Eom, C. B. Enhancement of Ferroelectricity in Strained BaTiO3 Thin Films. *Science* **2004**, *306*, 1005–1009.
- (19) Haeni, J. H.; Irvin, P.; Chang, W.; Uecker, R.; Reiche, P.; Li, Y. L.; Choudhury, S.; Tian, W.; Hawley, M. E.; Craigo, B.; Tagantsev, A. K.; Pan, X. Q.; Streiffer, S. K.; Chen, L. Q.; Kirchoefer, S. W.; Levy, J.; Schlom, D. G. Room-Temperature Ferroelectricity in Strained SrTiO<sub>3</sub>. *Nature* **2004**, *430*, 758–761.
- (20) Nagarajan, V.; Roytburd, A.; Stanishevsky, A.; Prasertchoung, S.; Zhao, T.; Chen, L.; Melngailis, J.; Auciello, O.; Ramesh, R.

- Dynamics of Ferroelastic Domains in Ferroelectric Thin Films. *Nat. Mater.* **2003**, 2, 43–47.
- (21) Yadav, A. K.; Nelson, C. T.; Hsu, S. L.; Hong, Z.; Clarkson, J. D.; Schlepuëtz, C. M.; Damodaran, A. R.; Shafer, P.; Arenholz, E.; Dedon, L. R.; Chen, D.; Vishwanath, A.; Minor, A. M.; Chen, L. Q.; Scott, J. F.; Martin, L. W.; Ramesh, R. Observation of Polar Vortices in Oxide Superlattices. *Nature* **2016**, *530*, 198–201.
- (22) Ivry, Y.; Lyahovitskaya, V.; Zon, I.; Lubomirsky, I.; Wachtel, E.; Roytburd, A. L. Enhanced Pyroelectric Effect in Self-Supported Films of BaTiO<sub>3</sub> with Polycrystalline Macrodomains. *Appl. Phys. Lett.* **2007**, 90, 172905.
- (23) Lu, D.; Baek, D. J.; Hong, S. S.; Kourkoutis, L. F.; Hikita, Y.; Hwang, H. Y. Synthesis of Freestanding Single-Crystal Perovskite Films and Heterostructures by Etching of Sacrificial Water-Soluble Layers. *Nat. Mater.* **2016**, *15*, 1255–1260.
- (24) Dong, G.; Li, S.; Yao, M.; Zhou, Z.; Zhang, Y. Q.; Han, X.; Luo, Z.; Yao, J.; Peng, B.; Hu, Z.; Huang, H.; Jia, T.; Li, J.; Ren, W.; Ye, Z. G.; Ding, X.; Sun, J.; Nan, C. W.; Chen, L. Q.; Li, J.; et al. Super-Elastic Ferroelectric Single-Crystal Membrane with Continuous Electric Dipole Rotation. *Science* 2019, 366, 475–479.
- (25) Nelson, C. T.; Gao, P.; Jokisaari, J. R.; Heikes, C.; Adamo, C.; Melville, A.; Baek, S. H.; Folkman, C. M.; Winchester, B.; Gu, Y.; Liu, Y.; Zhang, K.; Wang, E.; Li, J.; Chen, L. Q.; Eom, C. B.; Schlom, D. G.; Pan, X. Domain Dynamics during Ferroelectric Switching. *Science* **2011**, 334, 968–971.
- (26) Gao, P.; Britson, J.; Nelson, C. T.; Jokisaari, J. R.; Duan, C.; Trassin, M.; Baek, S.-H.; Guo, H.; Li, L.; Wang, Y.; Chu, Y.-H.; Minor, A. M.; Eom, C.-B.; Ramesh, R.; Chen, L.-Q.; Pan, X. Ferroelastic Domain Switching Dynamics under Electrical and Mechanical Excitations. *Nat. Commun.* **2014**, *5*, 3801.
- (27) Barzilay, M.; Qiu, T.; Rappe, A. M.; Ivry, Y. Epitaxial TiO<sub>x</sub> Surface in Ferroelectric BaTiO<sub>3</sub>: Native Structure and Dynamic Patterning at the Atomic Scale. *Adv. Funct. Mater.* **2019**, 1902549.
- (28) Li, D. B.; Strachan, D. R.; Ferris, J. H.; Bonnell, D. A. Polarization Reorientation in Ferroelectric Lead Zirconate Titanate Thin Films with Electron Beams. *J. Mater. Res.* **2006**, *21*, 935–940.
- (29) Hart, J. L.; Liu, S.; Lang, A. C.; Hubert, A.; Zukauskas, A.; Canalias, C.; Beanland, R.; Rappe, A. M.; Arredondo, M.; Taheri, M. L. Electron-Beam-Induced Ferroelectric Domain Behavior in the Transmission Electron Microscope: Toward Deterministic Domain Patterning. *Phys. Rev. B: Condens. Matter Mater. Phys.* **2016**, *94*, 174104.
- (30) Megaw, H. D. Crystal Structure of Barium Titanate. *Nature* **1945**, *155*, 484–485.
- (31) Barzilay, M.; Elangovan, H.; Ivry, Y. Surface Nucleation of the Paraelectric Phase in Ferroelectric BaTiO<sub>3</sub>: Atomic Scale Mapping. *ACS Appl. Electron. Mater.* **2019**, *1*, 2431–2436.
- (32) Schilling, A.; Adams, T.; Bowman, R.; Gregg, J.; Catalan, G.; Scott, J. Scaling of Domain Periodicity with Thickness Measured in BaTiO<sub>3</sub> Single Crystal Lamellae and Comparison with Other Ferroics. *Phys. Rev. B: Condens. Matter Mater. Phys.* **2006**, 74, 024115.
- (33) Lim, J.; Jung, H.; Baek, C.; Hwang, G. T.; Ryu, J.; Yoon, D.; Yoo, J.; Park, K. Il; Kim, J. H. All-Inkjet-Printed Flexible Piezoelectric Generator Made of Solvent Evaporation Assisted BaTiO<sub>3</sub> Hybrid Material. *Nano Energy* **2017**, *41*, 337–343.
- (34) Gao, P.; Liu, H. J.; Huang, Y. L.; Chu, Y. H.; Ishikawa, R.; Feng, B.; Jiang, Y.; Shibata, N.; Wang, E. G.; Ikuhara, Y. Atomic Mechanism of Polarization-Controlled Surface Reconstruction in Ferroelectric Thin Films. *Nat. Commun.* **2016**, *7*, 11318.
- (35) Barzilay, M.; Ivry, Y. Formation and Manipulation of Domain Walls with 2-nm Domain Periodicity in BaTiO<sub>3</sub> Without Contact Electrodes. *arXiv*; https://arxiv.org/abs/2002.06859v2 (accessed 2020-02-20).
- (36) Bhaskar, U. K.; Banerjee, N.; Abdollahi, A.; Wang, Z.; Schlom, D. G.; Rijnders, G.; Catalan, G. A. Flexoelectric Microelectromechanical System on Silicon. *Nat. Nanotechnol.* **2016**, *11*, 263–266.
- (37) Abdollahi, A.; Vásquez-Sancho, F.; Catalan, G. Piezoelectric Mimicry of Flexoelectricity. *Phys. Rev. Lett.* **2018**, 121, 205502.

(38) Ivry, Y.; Chu, D.; Durkan, C. Nanometer Resolution Piezoresponse Force Microscopy to Study Deep Submicron Ferroelectric and Ferroelastic Domains. *Appl. Phys. Lett.* **2009**, *94*, 162903. (39) Kalinin, V. S.; Kim, Y.; Fong, D. D.; Morozovska, A. M. Surface Screening Mechanisms in Ferroelectric Thin Films and Its Effect on Polarization Dynamics and Domain Structures. *Rep. Prog. Phys.* **2018**, *81*, 036502.